AIAA JOURNAL
Vol. 47, No. 12, December 2009

Ghost Fluid Method for Strong Shock Interactions Part 1: Fluid–Fluid Interfaces

Shiv Kumar Sambasivan* and H. S. UdayKumar†
The University of Iowa, Iowa City, Iowa 52242

DOI: 10.2514/1.43148

The interaction of shocks with multimaterial interfaces can occur in several applications, including high-speed flows with droplets, bubbles, and particles and hypervelocity impact and penetration. To simulate such complicated interfacial dynamics problems, a fixed Cartesian grid approach in conjunction with level-set interface tracking is attractive. In this regard, the ghost fluid method has been widely used to capture the interface dynamics. However, ghost fluid method experiences difficulties, particularly when strong shocks impinge on the interface. It has been shown that an accurate representation and decomposition of the wave systems (by solving a Riemann problem at the interface) significantly alleviates the shortcomings confronted by the ghost fluid method. Variants of the ghost fluid method proposed in the past differed in the way in which this Riemann problem was invoked at the interface. In this work, a simple, robust, and multidimensional procedure to construct the Riemann problem at the interface is presented. The work focuses primarily on resolving interface dynamics due to strong shocks interacting with embedded fluid–fluid interfaces (gas–gas and gas–liquid interfaces) in compressible flows. Several one- and two-dimensional problems involving moderate-to-very-large deformation of the embedded interface have been computed. The numerical examples demonstrate the flexibility, stability, and versatility of the approach in successfully resolving the embedded material interface.

I. Introduction

THE interaction of shocks with multimaterial interfaces is important in several applications, including high-speed flows with droplets [1], bubbles, and particles [2,3]; hypervelocity impact and penetration [4]; and detonation diffraction [5,6]. In such problems, simulations encounter challenges associated with the treatment of material interfaces, particularly when shocks and detonation waves impinge upon them. The result of such shock–interface interactions may be partial reflection, refraction, or transmission of the shocks and motion of the material interfaces under the influence of the shocked fields [7]. These motions can be large and may also lead to topological changes such as shattering, reconnection, collapse, etc. Accurate treatment and representation of these phenomena is the subject of the present paper.

High-resolution and higher-order schemes such as essentially nonoscillatory (ENO) [8] and weighted essentially nonoscillatory [9] perform very well for single-fluid media with discontinuities [10]. However, when such schemes are employed directly to solve multicomponent flows, undesirable oscillations in the form of pressure waves are prevalent near the material interface [11]. The difficulty resides in maintaining pressure equilibrium between the fluid components at the material interface, which results in computational inaccuracies and spurious oscillations [12]. Discontinuities such as shocks are nonlinear phenomena with converging characteristics and so the numerical errors generated are confined within the (smeared) discontinuity [13]. On the other hand, for contact discontinuities, the characteristics run parallel to each other and hence there is no steepening mechanism to counter the numerical dissipation of the errors generated near the discontinuity [14]. Thus, errors in treating the presence of embedded interfaces can permeate the solution away from the interface. To prevent these spurious oscillations when dealing with material discontinuities, care must be exercised when treating the embedded interfaces in a sharp manner.

Several methods have been proposed in the past to treat the presence of material interface in multicomponent flows [11,12,15–17]. These methods are based on the fact that a strictly conservative scheme will not be able to maintain pressure equilibrium across the material interface [16]. Abgrall et al. [15,16] solved a separate nonconservative transport equation to update the specific function ($\Gamma(\gamma) = 1/(\gamma - 1)$) for the mixture. Karni [12] used a nonconservative pressure evolution equation to compute the pressure near the material interface. Jenny et al. [17] proposed a thermodynamically consistent correction algorithm for the total energy. All of these methods fall under the category of front-capturing methods. A good review of such methods is given by Abgrall and Karni [16]. Although these methods are at least quasi-conservative, smearing of the interface is an inherent feature. Treating materials that are separated by distinct sharp interfaces (as in droplet/bubble dynamics) by reformulating the problem using a mixture model (with diffuse interfaces), and therefore as a single-component inhomogeneous medium, casts the onus on the continuum formulation while relieving the numerical techniques. However, treatment of interfaces as nonsharp or diffuse zones within a mixture formulation is not devoid of numerical problems. For example, across the interface of multiphase compressible flow (say, containing gas–liquid interfaces) there are jumps in material properties. There are also sharp changes in material behavior and constitutive laws: for example, in the equation of the state. When a shock is transmitted across an interface, failure to capture this discontinuous response of the contiguous materials results in severe numerical instabilities or unphysical flowfields. For example, if the interface is not treated as a sharp entity, due to the presence of numerical diffusion at the interface, a nonphysical zone with an artificially diffused density field will result [18]. In such situations, it becomes necessary to use an ad hoc equation of state (representing some nonphysical averaged material) to obtain a continuous pressure field [19]. This results in inaccurate wave interactions and boundary conditions corresponding to this nonphysical zone being enforced at the interface [20]. Nevertheless, it is important to point out that despite these shortcomings, in some instances (like the shattering of droplets/bubble under the impact of strong shocks [21,22]), the diffuse interface approach may still be the most judicious choice.

Received 9 January 2009; accepted for publication 17 August 2009.

*Graduate Student, Department of Mechanical and Industrial Engineering; ssambasi@engineering.uiowa.edu. Student Member AIAA.

†Professor, Department of Mechanical and Industrial Engineering; ush@engineering.uiowa.edu. Member AIAA (Corresponding Author).

Alternatively, front-tracking methods that preserve interfaces as sharp discontinuities retain the two fluid regions as separate entities but must contend with the numerical challenges of discretizing the governing equations to apply relevant boundary conditions on the interface. In recent times, the use of sharp interface methods for the representation of solid and fluid boundaries in incompressible [23–26] and compressible [4,20,27–30] flows has become popular. These methods are particularly attractive for the treatment of moving boundaries in the flow domain since grid generation and management are dispensed with. In this regard, the ghost fluid method (GFM) originally formulated by Fedkiw et al. [28] provides a simple framework to implicitly transmit the presence of an interface to the flowfield. The GFM requires the definition of a band of ghost fluid points corresponding to each phase of the interacting media. The band of ghost fluid points (when populated with suitable flow properties) together with its respective real fluid constitutes, in effect, a single flowfield. Thus, discretization schemes with uniform order of accuracy can be applied throughout the computational domain without requiring any special treatment near the interface. Hence, the implementation of the numerical scheme and the interface treatment are decoupled, and the onus is shifted to populating the ghost points with the appropriate flow properties.

GFM has been widely used to treat the presence of embedded fluid–fluid and solid–fluid interfaces [4,20,27–31]. However, these variants in GFM differ in the way in which the ghost points are populated. Fekdiw et al. [32] used GFM in the context of shock and detonation tracking. The Rankine–Hugoniot (R-H) jump conditions were solved across the discontinuity to populate the ghost points. In subsequent work, Fedkiw [27] and Caiden et al. [33] extended the GFM approach for coupling stiff and nonstiff fluids (gas–water interfaces). In this case, the ghost fluid states were defined by extrapolating the velocity at the interface in the water medium and the pressure from the air medium [27]. This approach, although attractive for gas–water interfaces, was not suitable to represent gas–gas interfaces. Aslam [34,35] proposed to construct a Riemann problem across discontinuities (shocks and contacts) and populate the ghost points by solving a Riemann problem normal to the interface. Liu et al. [20], clearly demonstrating the failure of the original GFM, proposed the modified GFM (MGFM). Attributing the failure of original GFM to inaccurate treatment of the wave interactions occurring at the interface, Liu et al. solved the local Riemann problem by carrying out characteristic analysis on the waves arriving at the interface. Later, Hu and Khoo [36] extended this approach by solving two separate Riemann problems: one for the real fluids and a second for the real and corresponding ghost fluid. By enforcing the condition that the two Riemann problems work in conjunction such that the pressure and the velocity obtained from the real–ghost interactions correspond to the real interactions [36], they were able to employ the isobaric fix to compute the density field for the ghost points. This approach was called interface-interaction GFM (IGFM). Both IGFM and MGFM were successfully applied to solve a multitude of problems involving strong shocks interacting with gas–gas and gas–water interfaces. Recently, Wang et al. [37] proposed a simple Riemann-solver-based ghost point construction procedure called the real GFM (rGFM). The rGFM was successfully applied to solve several one-dimensional and simple two-dimensional problems.

In this work, a simple but efficient method to construct the Riemann problem has been developed. The method is an extension of the approach formulated by Aslam [34,35] and is similar to the rGFM approach proposed by Wang et al. [37]. The method developed provides a uniform formulation to treat both fluid–fluid and solid–fluid interfaces. In the case of solid objects embedded in a compressible flow, it is well known that numerical schemes suffer from acute over- and underheating errors [38,39]. Several corrective measures have been developed to suppress the growth of such errors. A unified methodology should be able to suppress these over- and underheating errors and also accurately capture the wave interactions occurring at the interface. Hence, the focus of this work is on designing a simple yet robust method that can handle strong shock interactions with gas–gas, gas–water, and solid–fluid interfaces.

The approach adopted in this work has a multidimensional characteristic intrinsic to the construction procedure, making it attractive for three-dimensional applications. Briefly, a local Riemann problem is constructed at the interface, which is then solved using an exact Riemann solver. The resulting Riemann states obtained from solving the Riemann problem are used to populate the respective ghost points. In a separate work, this method is extended to treat embedded solid objects in compressible flows and has been shown to be effective in suppressing the over- and underheating errors [40]. As demonstrated in Sec. IV, the results obtained from the current simulations clearly indicate that the proposed method is consistent in generating satisfactory solutions for several complex configurations and shocks interacting with interfaces; shocks interacting with droplets, bubbles, and free surface have been computed. The method is currently being applied to study the dynamics of dense particulate compressible flows.

II. Governing Equations

The governing equations comprise a set of hyperbolic conservation laws. In Cartesian coordinates, the governing equations in two-dimensions take the following form:

$$\frac{\partial \mathbf{U}}{\partial t} + \frac{\partial \mathbf{F}}{\partial x} + \frac{\partial \mathbf{G}}{\partial y} = \Phi_A \mathbf{S} \tag{1}$$

where

$$\mathbf{U} = \begin{pmatrix} \rho \\ \rho u \\ \rho v \\ \rho E \end{pmatrix}, \qquad \mathbf{F} = \begin{pmatrix} \rho u \\ \rho u^2 + p \\ \rho u v \\ u(\rho E + p) \end{pmatrix}$$

$$\mathbf{G} = \begin{pmatrix} \rho v \\ \rho u v \\ \rho v^2 + p \\ v(\rho E + p) \end{pmatrix}, \qquad \mathbf{S} = -\frac{1}{x}\begin{pmatrix} \rho u \\ \rho u^2 \\ \rho u v \\ u(\rho E + p) \end{pmatrix}$$

Here, $E = e + \frac{1}{2}(u^2 + v^2)$ is the total internal energy and e is specific internal energy. For two-dimensional problems of interest, the switch function Φ_A is set to 0. For axisymmetric problems, the switch function Φ_A is set to 1. Closure for the above set of governing equations is obtained by using a stiffened equation of state [41,42]:

$$P = \rho e(\gamma - 1) - \gamma P_\infty \tag{2}$$

where γ is the specific heat ratio (also called a Grüneisen exponent [1] for stiff fluids) and P_∞ is a material-dependent constant [19]. For the case of ideal gas we have $\gamma = c_p/c_v$ and $P_\infty = 0$. For stiff fluids like water, the Grüneisen exponent and the material-dependent constant take the values of 5.5 and 0.613 GPa, respectively. From the definition of sound speed, we have

$$c^2 = \left(\frac{\partial P}{\partial \rho}\right)_{s=\text{constant}} \tag{3}$$

Using Eq. (2), the speed of sound then becomes

$$c = \sqrt{\frac{\gamma(P + P_\infty)}{\rho}} \tag{4}$$

III. Level-Set Method and Classification of Grid Points

Level sets, introduced by Osher and Sethian [43], are used to track and represent embedded boundaries. The level-set field is advected using the level-set advection equation [44,45]. A fourth-order ENO scheme for spatial discretization and a fourth-order Runge–Kutta time integration are used for solving the level-set advection equation. For other relevant details regarding the implementation of level-set methods the reader may refer to the original literature [43,46].

Table 1 A compendium of past literature that has reported the use of Riemann problem-based technique to resolve the presence of (shock/material) discontinuities in the flowfield

Reference	Year	Methodology
Davis [14]	1992	Solved an approximate Riemann problem across the interface using the method of characteristics approach. The solution from this approximate Riemann solver was then used to construct the second-order Godunov fluxes.
Cocchi and Saurel [18]	1997	Employed an exact Riemann solver to correct the numerical errors afflicting the interfacial points. The interfacial points suffering from numerical diffusion were treated using a combination of the solution obtained from the numerical scheme and Riemann problem.
Fedkiw et al. [32]	1999	Employed Riemann solver approach in the context of tracking shock and detonation fronts.
Aslam [34,35]	2001, 2003	Constructed a local Riemann problem normal to the (shock/material) discontinuity, to define the ghost states in the GFM frameworks.
Liu et al. [20]	2003	Developed the MGFM. The MGFM solved a local Riemann problem normal to the interface to define the ghost states.
Hu and Khoo [36]	2004	Extended the MGFM approach by solving two separate Riemann problems: one for the real fluids and a second for the real and corresponding ghost fluid.
Wang et al. [37]	2006	Developed the rGFM. The rGFM also employed a Riemann problem construction procedure to populate the ghost points.

The grid points on the Cartesian mesh can be classified as *bulk points* and *interfacial points*. The points that lie immediately adjacent to the interface are tagged as interfacial points, as shown in Fig. 1. If $\phi_{\text{curr}}\phi_{\text{nbr}} \leq 0$, where the subscript curr denotes the current point and nbr denotes the neighboring point, then the current and the neighboring point are tagged as interfacial points. All the other points are classified as bulk points. A band of ghost points are defined for each phase of the interacting media, as shown in Fig. 1. The ghost point band typically extends up to $4\max(\Delta x, \Delta y)$ distance from the interface. Again, the level-set field can be used to define the band of ghost points. The set of ghost points that are immediately adjacent to the interface are tagged as *interfacial ghost points*, similar to the regular interfacial points. Figure 1 shows the node classification for phase 1, and a similar classification exists for phase 2.

A. Ghost Fluid Method

The ghost fluid method was first proposed by Glimm et al. [47], later adopted by Fedkiw et al. [28], and is frequently employed to treat compressible flow problems with embedded interfaces. The GFM formulated by Fedkiw et al. provides a simple framework to inject the boundary conditions for sharp representation of discontinuities [29]. The central idea is the definition of a band of ghost points corresponding to each phase of the interacting materials. The ghost points can be defined based on the sign of the level-set field. Thus, effective communication with the flow solver can be achieved by suitably populating these ghost points with flow properties such that the real fluid together with the corresponding ghost field depict the interface properties and conditions precisely. For more details on the construction procedure and on the basic ideas of the ghost fluid method, the reader may refer to the original paper by Fedkiw et al. [28].

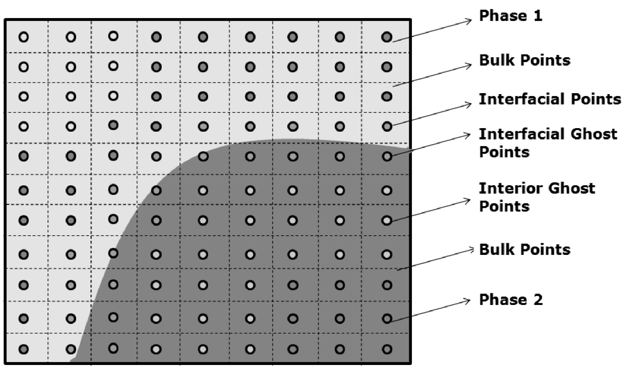

Fig. 1 Classification of grid points as bulk points, interfacial ghost points, and interior ghost points.

Fedkiw et al. [28] populated the ghost points based on the fact that the pressure and velocity are continuous across the contact discontinuity. This enables the pressure and velocity to be directly copied from the real fluid onto the ghost field. Since the entropy advects with material velocity (corresponding to the characteristic wave traveling with fluid/particle velocity), there is no entropy exchange between the two fluids. This allows the entropy to be extended to the ghost points (a procedure called isobaric fix by Fedkiw et al. [28]), which can then be used to compute the density for the ghost points. This simple approach was found to be robust for weak shocks interacting with the interface. However, when the shock strength and the material stiffness of the interacting fluids were increased considerably, it was found that this method failed to maintain a nonoscillatory pressure field. Liu et al. [20] pointed out the inability of the original GFM to accurately resolve the wave interactions at the interface. According to them, GFM essentially solves two separate single medium Riemann problems (real–ghost interaction Riemann problem) across the interface. The resolution of the waves from the real–ghost interaction does not always concur with the Riemann states generated from real fluid interactions [20]. Hence, with strong shocks impinging on interfaces with high impedance mismatch, this discrepancy in wave representation results in inaccurate shock and interface locations that result in unphysical oscillations in the flowfield [20].

B. Riemann Problem at the Interface

Carefully developed interface treatments can avoid the shortcomings of the original GFM by decomposing the singularities in the flowfield and material properties [20]. Interfacial states satisfying such conditions can be obtained by solving the R-H jump conditions at the material interface. The solution for the R-H jump conditions are obtained by constructing and solving a local Riemann problem normal to the interface. Table 1 provides a compendium of past literature in which the Riemann problem-based approach has been employed (both in the GFM and non-GFM framework) to resolve the presence of (shock/material) discontinuities in the flowfield.

The methods discussed in Table 1 differed in the way in which the Riemann problem was incorporated and solved at the interface. Along the same lines, the methodology developed in this work focuses on designing a simple yet robust method for constructing the Riemann problem normal to the interface. The method has multidimensional characteristics built in the construction procedure and is easy to implement. The method is an extension of Aslam [34,35] and has been shown here to successfully simulate strong shocks interacting with both gas–gas and gas–water interfaces. As will be

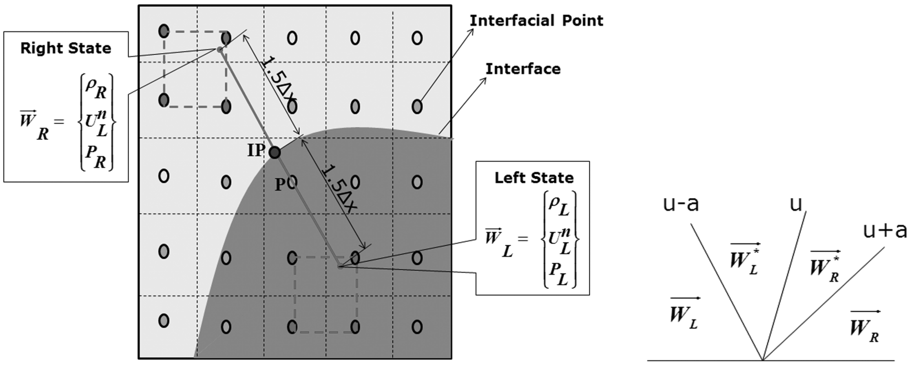

a) b)

Fig. 2 Illustrations of a) procedure to construct the Riemann problem at the interface and b) typical wave structure for the Riemann problem.

shown in Sec. IV.A.1, the approach adopted in this work has been shown to minimize and confine the associated conservation errors near the interface. In a separate work [40], this method has been shown to mitigate over- and underheating errors effectively and also to work consistently for a wide range of problems involving strong and weak shock interactions with embedded solid boundaries.

C. Constructing the Local Riemann Problem at the Interface

The aforementioned (GFM and non-GFM) sharp interface methods require the construction of a local Riemann problem normal to the interface. In this section, a simple method is presented to accomplish this task. From each interfacial point, such as point P in Fig. 2a, a probe is inserted in the normal direction to the interface. The coordinates of the point of intersection of the probe (from point P) and the interface (i.e., point IP on the interface in Fig. 2a), can be determined as follows:

$$\mathbf{X}_{\text{IP}} = \mathbf{X}_P + \mid \phi_P \mid \mathbf{N}_P \tag{5}$$

The left and the right states required for assembling the Riemann problem are obtained by advancing a distance of 1.5 Δx on either side of the interface from IP. The length of the probe (1.5 Δx) is chosen so that the interfacial point P, for which the Riemann problem is being constructed, bears no or minimal weight in the interpolation procedure involved in defining the Riemann problem. This enables the Riemann problem to be constructed with points that are not infused with the errors generated at the interface. To maintain consistency, the point that lies inside the level set is always denoted as the left state and the point that lies outside the level set is always denoted as the right state. Thus, the coordinates of the points corresponding to the left and right states can be computed as follows:

$$\mathbf{X}_L = \mathbf{X}_{\text{IP}} - 1.5\Delta x \mathbf{N}_P \tag{6}$$

$$\mathbf{X}_R = \mathbf{X}_{\text{IP}} + 1.5\Delta x \mathbf{N}_P \tag{7}$$

The flow properties $\mathbf{W}_{L|R}$ corresponding to the left $\mathbf{X}_L$ and the right $\mathbf{X}_R$ states can then be obtained using a simple bilinear interpolation procedure, as shown in Fig. 2a.

1. *Generalized Riemann Solver for Gas–Water Interface*

For the sake of completeness, the analytical solution for the Riemann problem is briefly described here. Once the Riemann problem is constructed, the solution for the initial value problem can be obtained using a suitable Riemann solver. In this case, the Riemann problem was solved exactly. A good discussion on standard procedures to solve the Riemann problem can be found in the book by Toro [48]. Haller et al. [1] and Cocchi et al. [19] outlined the procedure to solve the Riemann problem for a gas–water interface (based on stiffened equation of state). The solution for the Riemann problem consists of four states separated by three waves, as shown in Fig. 2b. The nonlinear characteristic waves (with wave speeds $u + a$ and $u - a$) can be either a shock wave or a rarefaction wave. The linear characteristic wave (which travels at the particle velocity u) represents the interface separating the interacting materials. The solution for the Riemann problem determines the intermediate $\star$ states sandwiching the interface (contact discontinuity), across which pressure and normal velocity are continuous but the density is discontinuous. Leaving the details pertaining to the steps for constructing the functions required to solve the Riemann problem to Toro [48], the functions and the algebraic equation are listed next:

$$f(p, \mathbf{W}_L, \mathbf{W}_R) = f_L(p, \mathbf{W}_L) + f_R(p, \mathbf{W}_R) + \Delta u^n = 0 \tag{8}$$

where $\Delta u^n = u^n_L + u^n_R$, and where $u^n_{L|R}$ are the normal velocity components, $\mathbf{W}_{L|R} = (\rho_{L|R}, u^n_{L|R}, p_{L|R})^T$, and

$$f_{L|R}(p, \mathbf{W}_{L|R})$$
$$= \begin{cases} f^{\text{rare faction}}_{L|R} & = \frac{2a_{L|R}}{\gamma_{L|R}-1}\{1 - (\frac{p^\star + p^{L|R}_\infty}{p^\star + p^{L|R}_\infty})^{\frac{\gamma_{L|R}-1}{2\gamma_{L|R}}}\} \text{ if } \frac{p^\star + p^{L|R}_\infty}{p^\star + p^{L|R}_\infty} < 1.0 \\ f^{\text{shock}}_{L|R} & = \sqrt{\frac{A_{L|R}}{B_{L|R} + (p^\star + p^{L|R}_\infty)}}(p^\star - p^{L|R}_\infty) \text{ if } \frac{p^\star + p^{L|R}_\infty}{p^\star + p^{L|R}_\infty} \geq 1.0 \\ A_{L|R} & = \frac{2}{(\gamma_{L|R}+1)\rho_{L|R}} \\ B_{L|R} & = (\frac{\gamma_{L|R}-1}{\gamma_{L|R}+1})(p_{L|R} + p^{L|R}_\infty) \end{cases}$$

2. *Correction Procedure*

The nonlinear algebraic equation (8) can be solved via Newton iterations to determine the intermediate states $\mathbf{W}^\star_{L|R}$. The intermediate states $\mathbf{W}^\star_{L|R}$ obtained from solving the Riemann problem are then used to correct the flow properties of the real fluid at the interfacial points. For instance, as shown in Fig. 3b, the Riemann state $\mathbf{W}^\star_L$ obtained from solving the Riemann problem constructed at the interfacial point P is used to correct the flow properties of the real fluid at point P. This will ensure that a constant entropy field is maintained throughout the interacting materials (except across shocks). This in turn prevents the diffusion of the entropy field across the interface and hence prohibits entropy exchange between the interacting (real) fluids. It was pointed out earlier in Sec. III.A that a simple extension of the entropy field to correct the real fluid properties at the interfacial points does not comply with the nature of the characteristic waves arriving/leaving the interface. On the contrary, the correction procedure enforced in the current approach account for the wave systems interacting with the interface.

3. *Populating the Ghost Points*

Once the flow properties at the interfacial points are corrected, the flow properties are extended along the normal direction to the interface to populate the respective interior ghost points. To carry out the multidimensional extrapolation procedure, the partial differential equation given in Eq. (9) is solved to steady state:

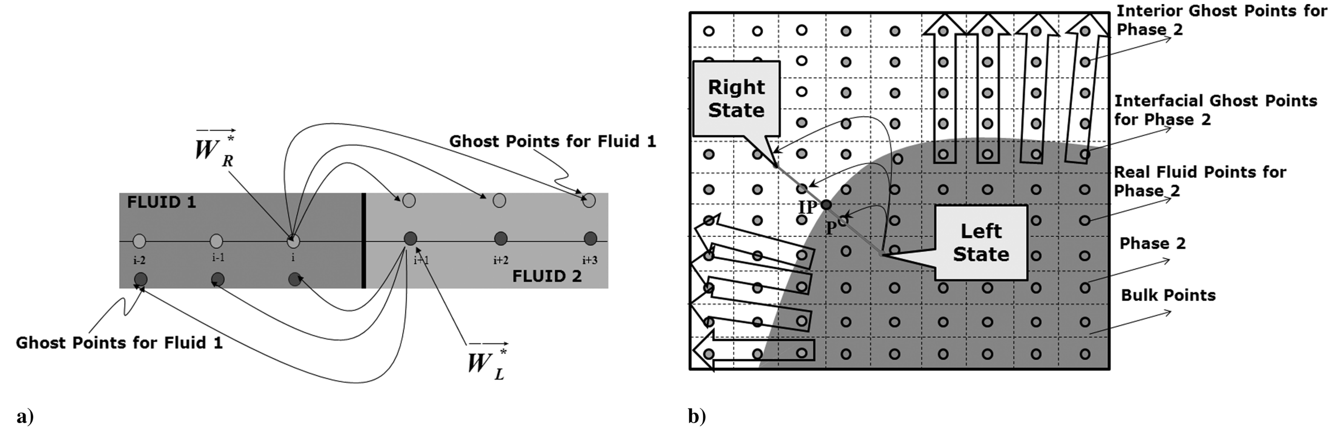

Fig. 3 One- and two-dimensional correction and extrapolation procedure.

$$\frac{\partial\Psi}{\partial\tau} + H(\phi_l)\mathbf{n}\cdot\nabla\Psi = 0 \tag{9}$$

where Ψ is the variable extended across the interface, τ is the pseudotime, and $H(\phi_l)$ is the unit Heaviside function defined as

$$H(\Psi) = \begin{cases} 0 & \text{if } \phi_l \leq 0.0, \\ 1 & \text{if } \phi_l > 0.0 \end{cases}$$

The variable ϕ_l used in the above equations denotes the value of the level-set distance function for the lth embedded interface. In the current work, the variable Ψ extended across the interface corresponds to the flow properties at the intermediate state $\mathbf{W}^\star_{L|R}$ obtained from solving the Riemann problem. As given in Eq. (9), a constant-extrapolation method is used for populating the ghost points, although higher-order extrapolation procedures are possible [49]. The one-dimensional version of the correction and the extension procedure is shown in Fig. 3a. Figure 3b shows the corresponding multidimensional correction and extension procedure carried out along the normal direction to the interface. It is important to note that the velocity obtained from the Riemann solver corresponds to the normal velocity component computed in the local curvilinear coordinate. To reconstruct the velocity vector in the global Cartesian coordinates, the slip condition at the interface is enforced. Thus, the tangential velocities computed for the Riemann problem (the left and the right states) are extrapolated across the interface. Accordingly, the velocity vector can be reconstructed as

$$\mathbf{u}^\star_L = u^{n\star}\hat{n} + \mathbf{u}^t_L \tag{10}$$

$$\mathbf{u}^\star_R = u^{n\star}\hat{n} + \mathbf{u}^t_R \tag{11}$$

where $\hat{n}$ is the normal vector, $u^{n\star}$ is the normal velocity obtained from the Riemann solver, and $\mathbf{u}^t_{L|R}$ are the tangential velocities (corresponding to the left and right states of the Riemann problem) computed as follows:

$$\mathbf{u}^t_L = \mathbf{u}_L - (\mathbf{u}_L\cdot\hat{n})\hat{n} \tag{12}$$

$$\mathbf{u}^t_R = \mathbf{u}_R - (\mathbf{u}_R\cdot\hat{n})\hat{n} \tag{13}$$

The velocity vector can then be decomposed into its corresponding components (u, v, w) in the Cartesian coordinates.

D. Freshly Cleared Cells

As the interface sweeps through the computational domain, a computational point that was previously inside the object (i.e., belonging to, say, phase 1) may now lie outside the object (i.e., belonging to phase 2) and vice versa. Identification of these points is straightforward once the level-set field is updated. Explicitly, points for which $\phi^n_i\phi^{n+1}_i < 0$ are tagged as freshly cleared cells. Although the values with which the freshly cleared cells are populated are temporary (as they are overwritten in the correction procedure), depending on the location of these points, they may or may not participate in the interpolation procedure involved in constructing the Riemann problem. Hence, it is required to update the flow and material properties belonging to these points at the beginning of each time step. There are several ways to update the properties of the freshly cleared cells. The easiest and the most direct method in the GFM framework adopted in this work is to copy the properties of ghost fluid variables at that point onto the real fluid properties.

IV. Numerical Examples

In this section, several numerical examples will be presented to demonstrate the capabilities of the current approach. The Euler equations (1) were solved using a third-order total variation diminishing (TVD)-based Runge–Kutta scheme for time integration and third-order convex ENO scheme [50] for spatial discretization. Details pertaining to the implementation of the convex ENO scheme in the current context are given by Tran and UdayKumar [4]. The governing equations were nondimensionalized based on freestream density ρ_∞, pressure p_∞, and the sonic velocity $a_\infty = \sqrt{p_\infty/\rho_\infty}$. Unless otherwise stated, the atmospheric conditions are chosen to nondimensionalize the governing equations. A suitable length scale is chosen depending on the dimensions of the immersed object, and the grid spacing for one-dimensional simulations was set at $\Delta x = 1/200$ unless stated to the contrary. Numerical schlieren images shown in this section were generated using the method outlined by Quirk and Karni [3]. It is worth mentioning here that the term R-GFM used in this section corresponds to Riemann–GFM and not to be confused with the rGFM approach of Wang et al. [37].

A. One-Dimensional Example

In this section, a series of one-dimensional shock-tube (of unit length) problems are presented. The initial condition corresponds to a singularity in flow variables that resolves into a transmitted and a reflected shock or expansion wave or both (depending on the impedance mismatch between the interacting fluids) and a contact discontinuity. The resulting contact discontinuity is tracked and represented as a sharp interface using the GFM approach.

1. *Example 1*

An example of a multimaterial shock-tube problem is the one-dimensional air–helium shock tube with the initial conditions given next:

$$(\rho, P, u, \gamma) = \begin{cases} (1.0, 1.0, 0.0, 1.4) & \text{for } x < 0.5 \\ (0.125, 0.1, 0.0, 1.667) & \text{for } x \geq 0.5 \end{cases}$$

The plots of density, pressure, velocity, and entropy after 100 time steps are displayed in Fig. 4. As in the previous case, both versions of

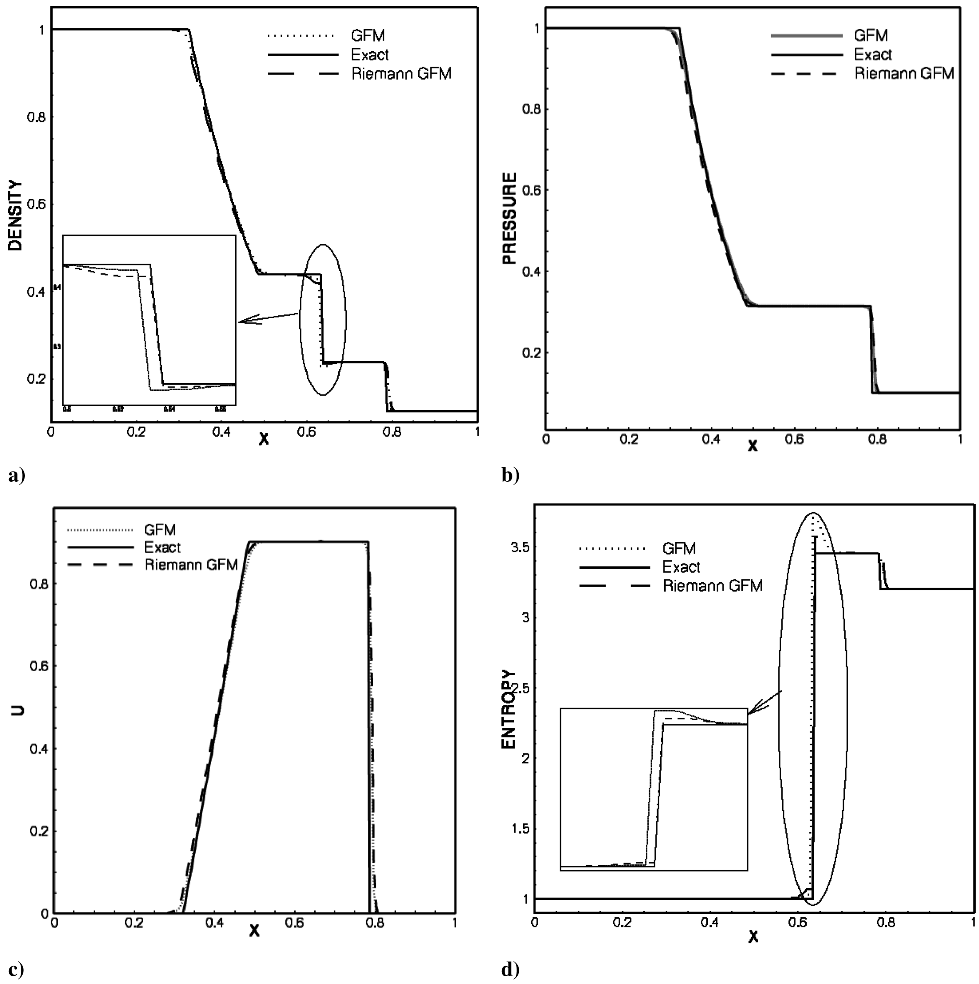

Fig. 4 Example 1: plots for the air–helium shock-tube problem. The inserts correspond to the zoomed-in view of the variation close to the interface.

GFM underpredict the density near the interface. The insert shows the zoomed-in view of the density profile close to the interface. The interface position predicted by original GFM is shifted by two/three grid points relative to the exact solution. In contrast, the interface location predicted by the R-GFM approach is in line with the exact solution. The pressure and the velocity plots also show good agreement with the exact solution. The entropy plots show modest overheating errors at the interface.

A conservation error analysis was carried out for this problem. The total mass, momentum, and energy conservation errors computed using the approach outlined by Wang et al. [37] are presented in Fig. 5. It was found that the conservation errors were noticeable only during the initial four–five time steps, when the shock wave was in the vicinity of the interface. This is consistent with the trend observed by Liu et al. [20] and Hu and Khoo [36]. The conservation errors observed in this case are mainly due to the errors that are inherent in the GFM approach. These errors arise from the numerical flux computed based on the ghost field. The numerical flux computed at the interface does not ensure strict conservation. As shown in Fig. 6, for all the bulk points, explicit numerical flux conservation can be achieved easily. On the other hand, due to the ghost fluid treatment from each side of the interface and the construction of fluxes using the ghost field, it is not possible to compute a unique numerical flux crossing the cell boundary for the interfacial points. The errors generated due to the nonuniqueness in the numerical flux computed at the interface becomes significant when strong shocks or detonation waves impinge on the interface.

It was pointed out by Abgrall and Karni [16] that a nonoscillatory pressure field can be produced by methods that are not strictly conservative at the interface. Because of the intrinsic nature of the ghost fluid treatment, where the ghost field is populated via extension from the real fluid, it is not straightforward to devise a scheme in the ghost fluid framework that would completely annihilate these conservation errors. However, Glimm et al. [13] attempted to construct conservative fluxes by locally rearranging the cells cut by the interface and explicitly enforcing appropriate jump conditions to guarantee equality of the numerical fluxes at the cell interface. This procedure of dynamically removing the conservation errors at the interface is appealing and feasible for one-dimensional problems but becomes extremely complicated when extended to multidimensional problems. A relatively simpler approach was proposed by Nguyen et al. [51]. In this approach, the conservation errors were alleviated by redistributing these errors to the numerical fluxes computed at the interface, at the end of each Runge–Kutta (RK) substep. As pointed out by Hu and Khoo [36], it is not readily apparent that such a postprocessing measure to correct the conservation errors is effective, particularly when conservation errors have already been incurred in the previous RK time step. In this work, no such additional measures were enforced to conserve the numerical fluxes at the interface. Furthermore, the conservation error analysis carried out in this work points out that these errors are confined to very few time steps when the shock resides on/near the interface and were found to be benign from the viewpoint of stable computation over the overall time of calculation. As shown in the insert in the density plots, both the interface and the shock locations are captured to a good degree of accuracy, indicating that the conservation errors involved are spatially and temporally localized (close to the interface and to the duration of shock–interface coincidence) and do not pollute the bulk of the solution or the long-term evolution of the flowfield.

2. *Example 2*

An example of a shock-tube problem with a gas–water interface is taken from Hu et al. [36,52]. The initial conditions are modified as

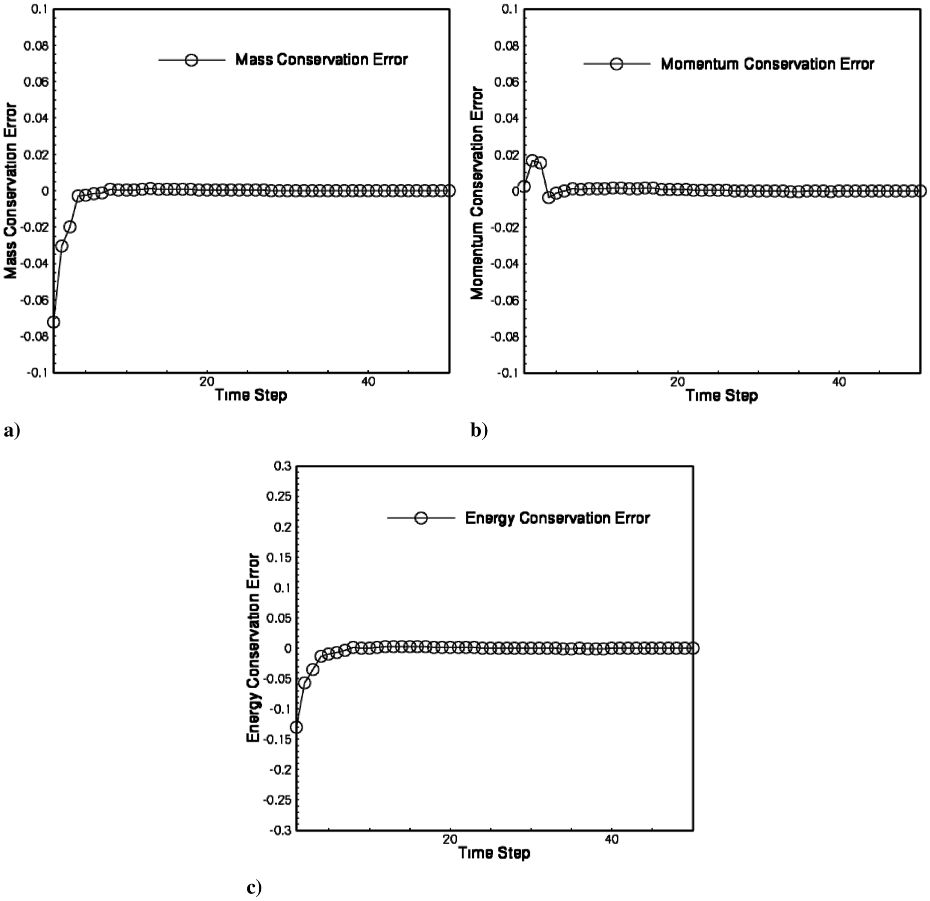

a) b)

c)

Fig. 5 Plots of conservation errors for the air–helium shock-tube problem.

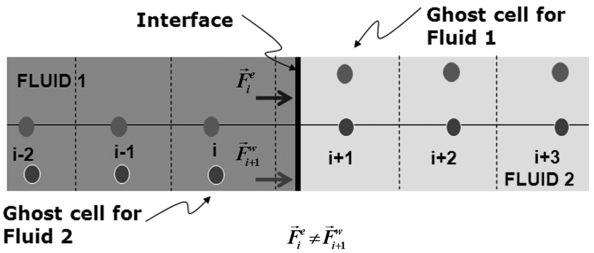

Fig. 6 Nonuniqueness in the numerical flux computed at the interface; figure reproduced from Abgrall and Karni [16].

$$(\rho, P, u, \gamma) = \begin{cases} (0.5, 20000.0, 100.0, 2.5) & \text{for } x < 0.5 \\ (1.0, 1.0, 0.0, 4.4) & \text{for } x \geq 0.5 \end{cases}$$

For the given conditions, a strong shock is both reflected and transmitted. Figure 7 shows the plots obtained after 200 time steps. Figure 7 shows that both the reflected and the transmitted shock locations are captured correctly. The position of the contact discontinuity matches very well with that of the exact solution. These features indicate that the conservation errors generated, even in the case of stiff fluids, are small. Because of very large entropy disparities between the interacting media, the entropy plots do not reveal any significant over- and underpredictions of the flow properties.

3. Example 3

The next example considered is a water–air shock-tube problem. The water medium is on the high-pressure side and the air is maintained at ambient condition. The initial conditions normalized with respect to the ambient conditions of water are given next:

$$(\rho, P, u, \gamma) = \begin{cases} (1.3, 10000.0, 0.0, 4.4) & \text{for } x < 0.5 \\ (0.001, 1.0, 0.0, 1.4) & \text{for } x \geq 0.5 \end{cases}$$

In this example, the shock wave travels from the water side into the air side and hence can be categorized as a fast–slow interface [53]. Because of high impedance mismatch, a strong rarefaction wave is reflected in the water medium and a weak shock wave is transmitted in the air medium. Figure 8 shows the plots obtained after 200 time iterations. The transmitted shock is extremely weak (the pressure ratio across the reflected rarefaction wave is much larger than the pressure ratio across the transmitted shock wave) and hence not readily visible from the density or pressure plots (Figs. 8a and 8b). However, the entropy plots shown in Fig. 8d show the jump across the transmitted shock in air. Also revealed by the entropy plots are the overheating errors. Although the overheating errors observed in this case are relatively large in magnitude, they are not significant enough to afflict the global solution. The computed position of the transmitted shock wave and the reflected expansion wave match well with the exact solution.

It is clear from the examples shown above that the R-GFM approach developed in this work is able to accurately resolve strong shock interactions with both gas–gas as well as gas–water interfaces. The methodology developed in this work is found to be robust and accurate in resolving multimaterial interfaces without requiring special treatments at the interface. The plots shown in Fig. 5 clearly indicate the conservation errors and the resulting under and overheating errors incurred are localized close to the interface.

B. Two-Dimensional Examples

1. Spherical Riemann problem

First in the multidimensional test cases presented in this work is the single-phase spherical Riemann problem. The initial conditions for this problem are given next:

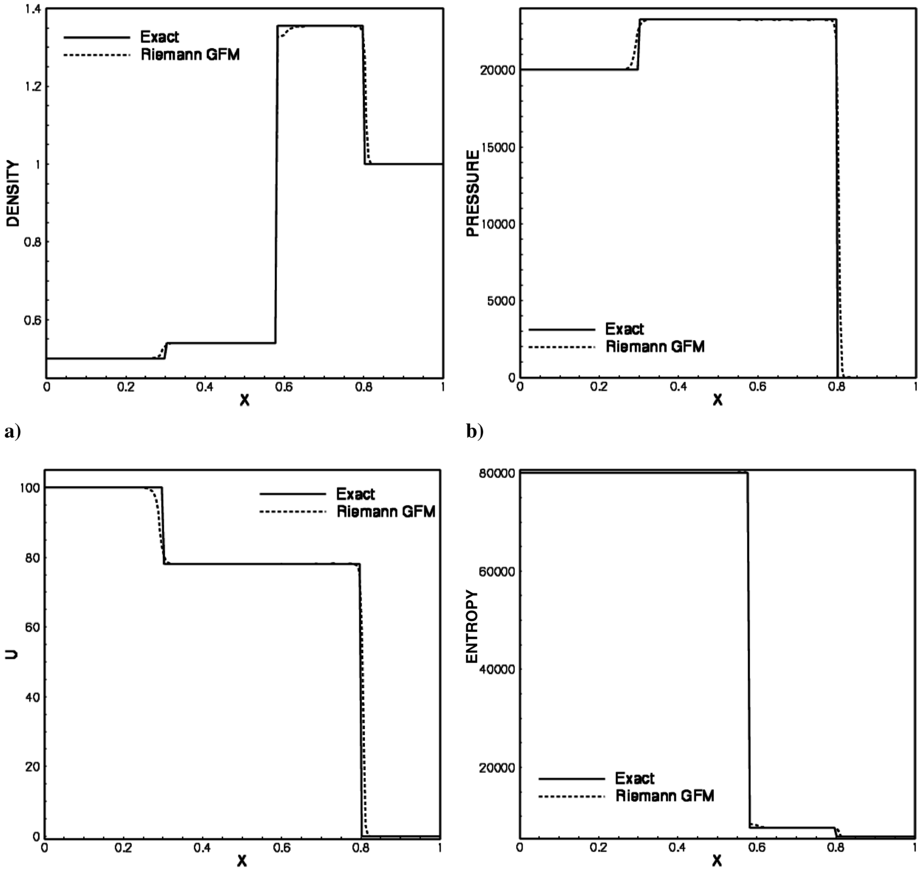

a) b) c) d)

Fig. 7 Example 2: plots for the gas–water shock-tube problem.

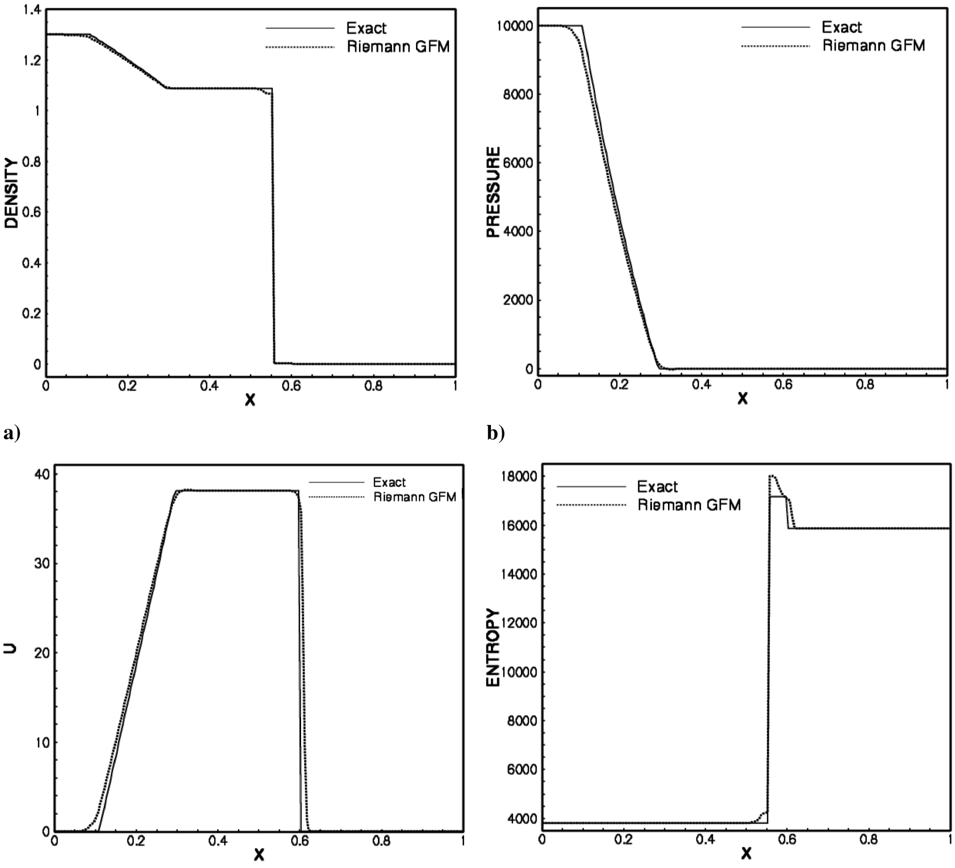

a) b) c) d)

Fig. 8 Example 3: plots for the water–air shock-tube problem.

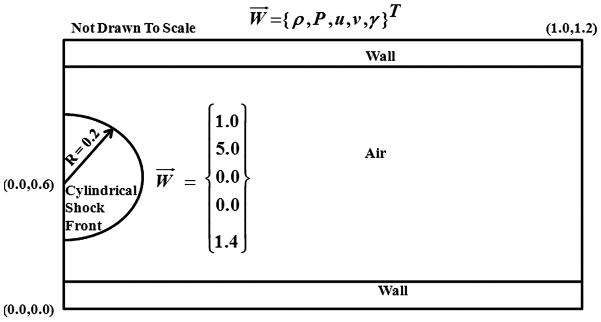

Fig. 9 Initial configuration for single-phase spherical Riemann problem.

$$(\rho, P, u, v, \gamma) = \begin{cases} (1.0, 5.0, 0.0, 0.0, 1.4) & \text{for } \sqrt{x^2 + (y - 0.5)^2} \leq 0.2 \\ (1.0, 1.0, 0.0, 0.0, 1.4) & \text{otherwise} \end{cases}$$

The one-dimensional problem in spherical coordinates is reconstructed in cylindrical coordinates (axisymmetric form), as shown in Fig. 9. Euler equations in axisymmetric form were solved in a 1.5 × 1.2 domain with 600 × 450 points. The simulations were carried out both with (R-GFM) and without explicit interface treatment (i.e., using ENO shock-capturing) for the contact discontinuity. The simulations were carried out until $T = 0.8$ units. The initial condition corresponds to a jump in pressure in the radial direction. This results in an inward-moving expansion wave, an outward-moving shock wave, and a contact discontinuity. Figure 10 shows that the R-GFM is able to resolve the contact discontinuity accurately without modifying the overall wave structures and their relative positions. The solution obtained from the R-GFM closely follows the trend observed by the shock-capturing schemes with no explicit interface treatment. Moreover, the enforcement of the sharp interface treatment accentuates weak features that are lost in the single-field simulation. As pointed out by Langseth and Leveque [54], the nonphysical zone developed due to wave focusing is visible at the center in both solutions. For a quantitative comparison, the variation of density and pressure along the centerline (at $y = 0.6$) at $t = 0.5$ are shown in Fig. 11. The plots are in close agreement with each other.

2. *Shock Interacting with Cylindrical Helium Bubble in Air*

a Case A: Mach 1.22 Shock Interacting with Helium Bubble in Air. The interaction of shock waves with gas bubbles has applications ranging from astrophysics [55,56] to cavitation damage of human tissue (shock wave lithotripsy) [57]. The example

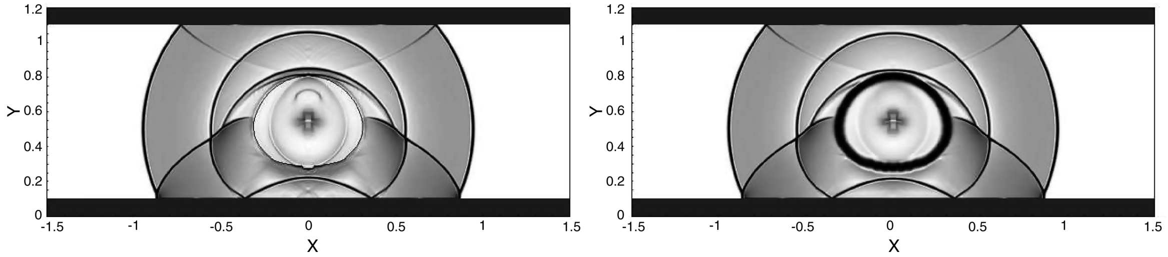

a) *t*=0.5, R-GFM **b) *t*=0.5, shock-capturing scheme (without GFM)**

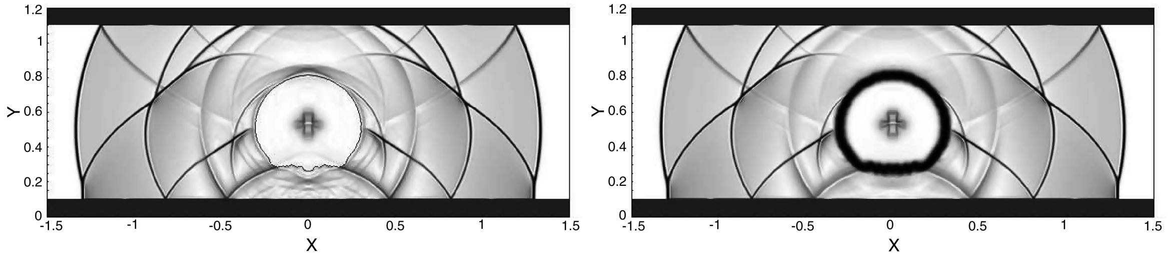

c) *t*=0.8, R-GFM **d) *t*=0.8, shock-capturing scheme (without GFM)**

Fig. 10 Snapshots of numerical schlieren image obtained with (left) and without (right) GFM treatment for the initially spherical contact discontinuity corresponding to time.

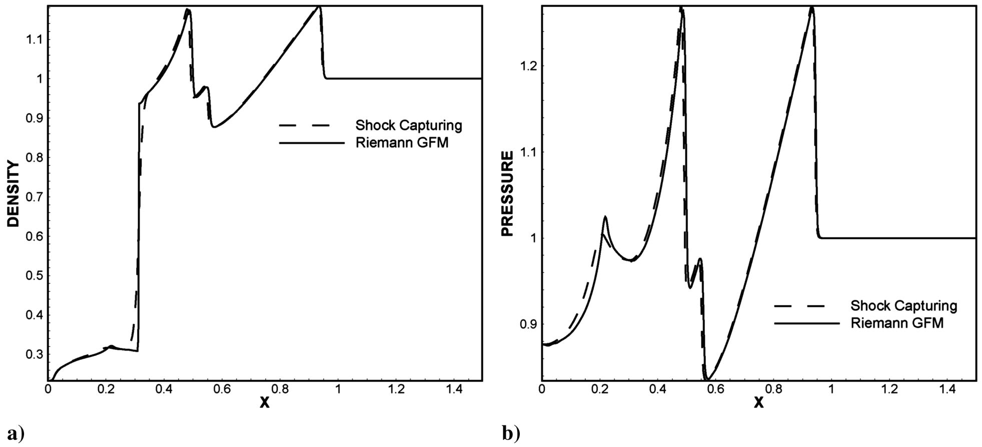

a) **b)**

Fig. 11 Comparison of a) density and b) pressure variation for spherical Riemann problem at $y = 0.6$ at $t = 0.5$.

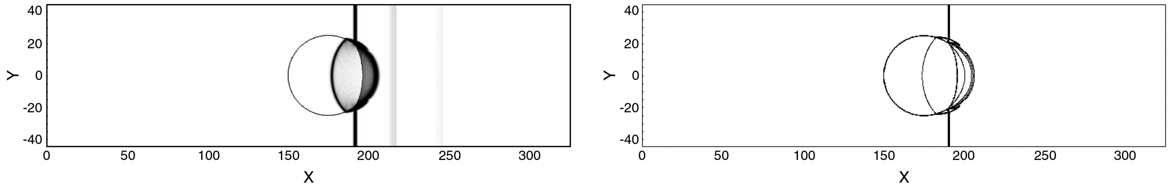

a) Numerical schlieren image at *t* = 85 *μs*

b) Density contours at *t* = 85 *μs*

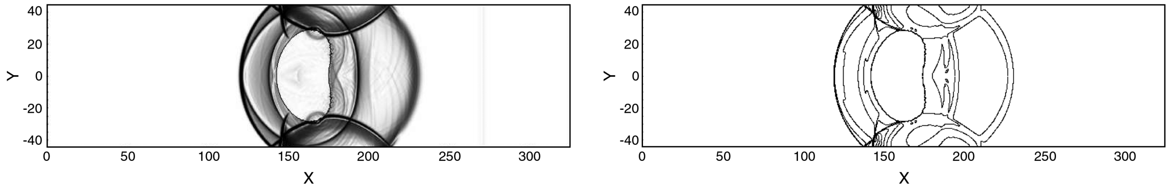

c) Numerical schlieren image at *t* = 188 *μs*

d) Density contours at *t* = 188 *μs*

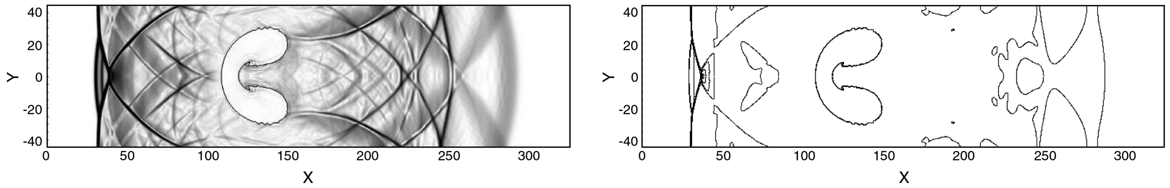

e) Numerical schlieren image at *t* = 188 *μs*

f) Density contours at *t* = 188 *μs*

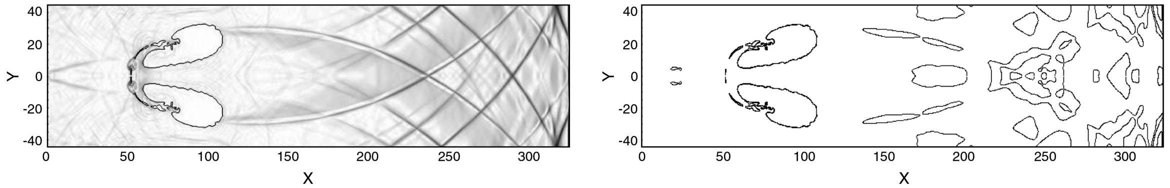

g) Numerical schlieren image at *t* = 803 *μs*

h) Density contours at *t* = 803 *μs*

Fig. 12 Snapshots of numerical schlieren image (left) and the corresponding density contours (right) at different instants in time for a Mach 1.22 shock impinging on a cylindrical He bubble.

considered in this section corresponds to the interaction of a Mach 1.22 shock with a cylindrical helium bubble in air. The configuration of this multicomponent system provides a weak shock interacting with fluids of varied stiffness. Haas and Sturtevant [58] considered shock waves interacting with R-22 refrigerant and helium bubbles. They provided a series of experimental observations that were later verified numerically by Quirk and Karni [3] and several others [11,22,28,36,59]. The initial problem configuration is given by Fedkiw et al. [28]. The initial conditions normalized based on the property of air at 1 atm and a length scale of 1 mm are

$$(\rho, P, u, v, \gamma) = \begin{cases} (1.3764, 1.5698, -0.394, 0.0, 1.4) & \text{for postshocked air, } x \geq 225 \\ (1.0, 1.0, 0.0, 0.0, 1.4) & \text{for preshocked air} \\ (0.138, 1.0, 0.0, 0.0, 1.667) & \text{for } \sqrt{(x-150)^2 + y^2} \leq 25 \end{cases}$$

The top and bottom of the domain are prescribed with reflective boundary conditions. The right end of the domain is prescribed with a Dirichlet inflow condition corresponding to postshocked air and the left end with Neumann outflow condition. The grid spacing $\Delta x = 0.25$.

As the speed of sound in helium is faster than in the surrounding air, the system can be classified as a slow-fast interface [60]. Hence, the impinging shock results in a refracted shock wave and a reflected rarefaction wave. As mentioned in Johnsen et al. [11], the refracted shock, upon reaching the other end of the bubble, further degenerates into a weaker reflected shock wave and a transmitted shock in air. This process of reflection continues until the resulting wave system degenerates into a weaker wave system [11]. The numerical schlieren image and density contours generated from the current simulation are shown in Fig. 12. Figures 12a and 12b show the transmitted shock wave and the reflected expansion. It is clear from the figure that the refracted shock inside the helium bubble travels faster than the incident shock. Figures 12c and 12d show the transmitted wave from the helium bubble and the incident shock in air. The multiply reflected weak wave system inside the helium bubble is also clearly visible. A closer examination of the figure depicts the initial stage of jet formation at the center of the bubble. The jet becomes more clearly visible in Figs. 12e and 12f. The bubble has now taken the familiar kidney bean shape. Not so readily visible features in Figs. 12e and 12f are the Kelvin–Helmholtz instability [22] reported on the surface of the bubble. These features may become evident with increase in mesh resolution. Finally, in Figs. 12g and 12h, the bubble is shattered into fragments due to the impact of the jet. It is worth noting that the giant vortical structures reported by Marquina et al. [22] are not readily visible in the current simulation. The reason is that Marquina et al. used an extremely fine mesh (8000 x 600) and a front-capturing technique that adds sufficient amount of numerical diffusion at the interface to capture these vortical structures and the associated Kelvin–Helmholtz instability.

b. Case B: Mach 6 Shock Interacting with Helium Bubble in Air. In this example, the Mach number of the impinging shock wave is increased to $M = 6$. The configuration of the system, including the domain boundary conditions and the grid resolution, are the same as in the previous case. The initial conditions are modified as

$$(\rho, P, u, v, \gamma) = \begin{cases} (5.268, 41.83, -5.752, 0.0, 1.4) & \text{for postshocked air, } x \geq 225 \\ (1.0, 1.0, 0.0, 0.0, 1.4) & \text{for preshocked air} \\ (0.138, 1.0, 0.0, 0.0, 1.667) & \text{for } \sqrt{(x-150)^2 + y^2} \leq 25 \end{cases}$$

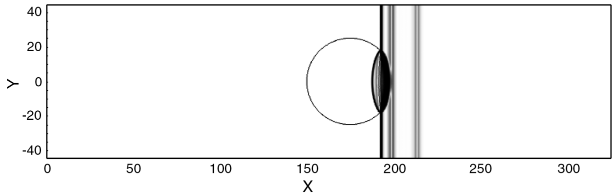

a) Numerical schlieren image at $t = 15.3$ μs

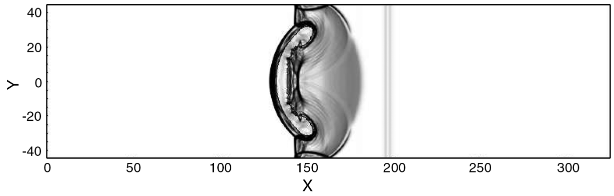

b) Numerical schlieren image at $t = 38.25$ μs

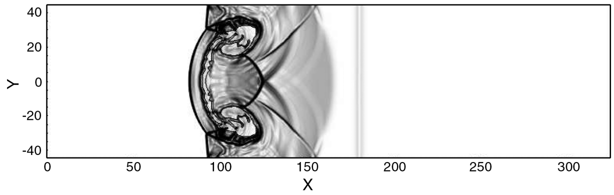

c) Numerical schlieren image at $t = 61.2$ μs

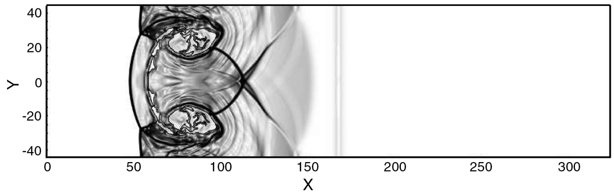

d) Numerical schlieren image at $t = 78$ μs

Fig. 13 Snapshots of numerical schlieren image for a Mach 6 shock interaction with a cylindrical He bubble at different instants in time.

Bagabir and Drikakis [59] analyzed the response of a gas bubble to shocks of different strengths. In their work, the computations were carried out for a single-component flow (with $\gamma = 1.4$) system. Hu et al. [52] carried out the corresponding multicomponent flow simulation with a helium bubble and air. The snapshots of the numerical schlieren image from the current simulations are displayed in Fig. 13. Since the refracted shock wave travels faster inside the bubble, it reaches the rear end of the bubble before the incident shock wave. The shock wave is then transmitted to the air medium, which is at rest. In the previous case, this transmitted shock wave coalesces with the incident shock wave to form a single planar shock wave that travels in the air medium. In this case, because of the time lag developed due to greater celerity of shock wave inside the bubble, the incident shock wave cannot coalesce with the transmitted shock wave, leaving behind a curved shock front from the transmitted shock attached to the planar incident shock wave. The strength of the incident shock is high enough to impart sufficient momentum to the helium bubble to drag the bubble along with it. As a result of this, the location of the shock and the interface are always in close proximity to each other. Moreover, the resultant changes on the topology of the interface are so intricate that the bubble shatters into tiny fragments due to the impact of the jet. The topology of the interface at different instants in time are displayed in Fig. 14. At time $t = 15.3$ μs, the transmitted shock deforms the front portion of the bubble, leaving the leeward side unaffected. At $t = 38.25$ μs, the shock has traversed most part of the bubble, and at time $t = 61.2$ μs, the bubble starts to deform. At $t = 78$ μs, the bubble has deformed

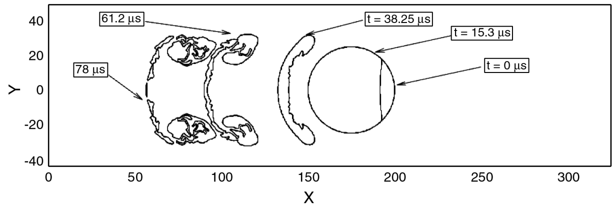

Fig. 14 Topology of the interface (zero level-set field) at different instants in time.

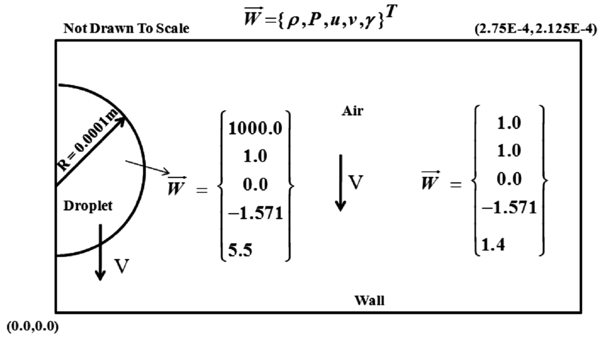

Fig. 15 Initial configuration for high-speed droplet impacting a flat substrate.

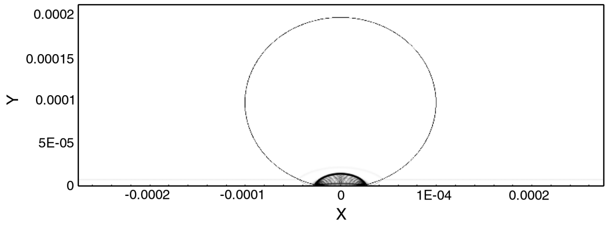

a) Numerical schlieren image at 21.7 ns

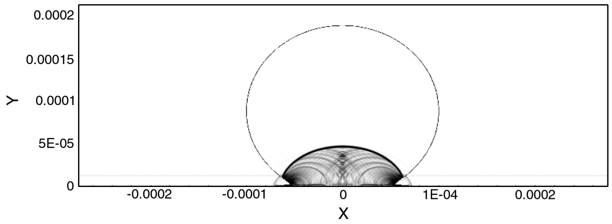

b) Numerical schlieren image at 37.54 ns

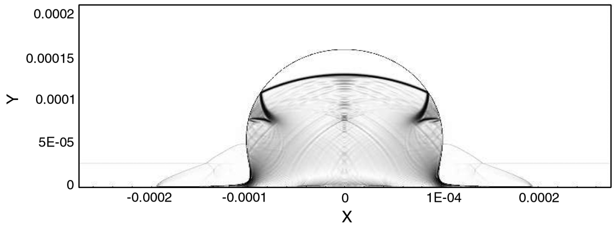

c) Numerical schlieren image at 84.32 ns

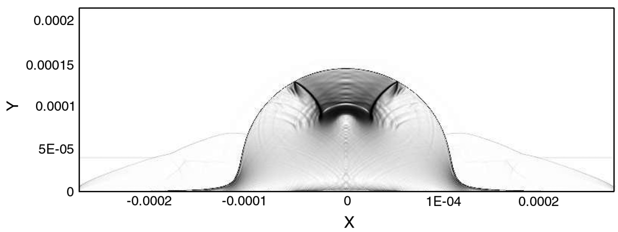

d) Numerical schlieren image at 118.8 ns

Fig. 16 Snapshots of numerical schlieren image illustrating the wave patterns generated from the impact of a high velocity droplet on a flat substrate at different instants in time.

completely and starts to form fragments. Once such fragments are formed, it is not possible to continue the simulation without employing special mesh enrichment techniques. Hu et al. [52] carried out their simulation by explicitly deleting small pockets of mass. No such additional measures were taken in this work; given the limitations of a uniform nonadaptive mesh, the results obtained are in close agreement with that of Hu et al. In an ongoing effort, local mesh refinement [61] technique is being employed to resolve the interface topology more accurately, and the results of this work will be reported in the future.

3. *High-Speed Impact of a Liquid Droplet*

In this example, high-speed impact of a liquid droplet over a flat substrate is considered. Impact of high-speed droplets and the resultant wave mechanisms are important in thermal spray and coating technologies [1,62]. A 200-μm-diam liquid droplet is injected with a high velocity of 500 m/s toward a rigid flat substrate located at the bottom. The initial conditions normalized with respect to the properties of surrounding air are given next:

$$(\rho, P, u, v, \gamma) = \begin{cases} (1000.0, 1.0, 0.0, -1.571, 5.5) & \text{for the liquid droplet,} \\ (1.0, 1.0, 0.0, -1.571, 1.4) & \text{for the surrounding air} \end{cases}$$

Figure 15 shows the geometrical setup for this problem. The left boundary is prescribed with a symmetry condition and the bottom boundary is prescribed with a reflective wall boundary condition. The top and the right boundaries are prescribed with a Neumann condition. Euler equations in the axisymmetric form are solved. Haller et al. [1,63–65] provided a detailed survey of this problem. They provided theoretical predictions for the jetting time that matched well with their corresponding numerical model. However, it is not clear from their analysis how the surrounding air was modeled. In this example, the flow inside the droplet as well as in the surrounding air is considered; that is, both the droplet and the surrounding air are injected with the same velocity toward the wall. The snapshots of the numerical schlieren image from the current simulation are shown in Fig. 16. The figures indicate that most of the

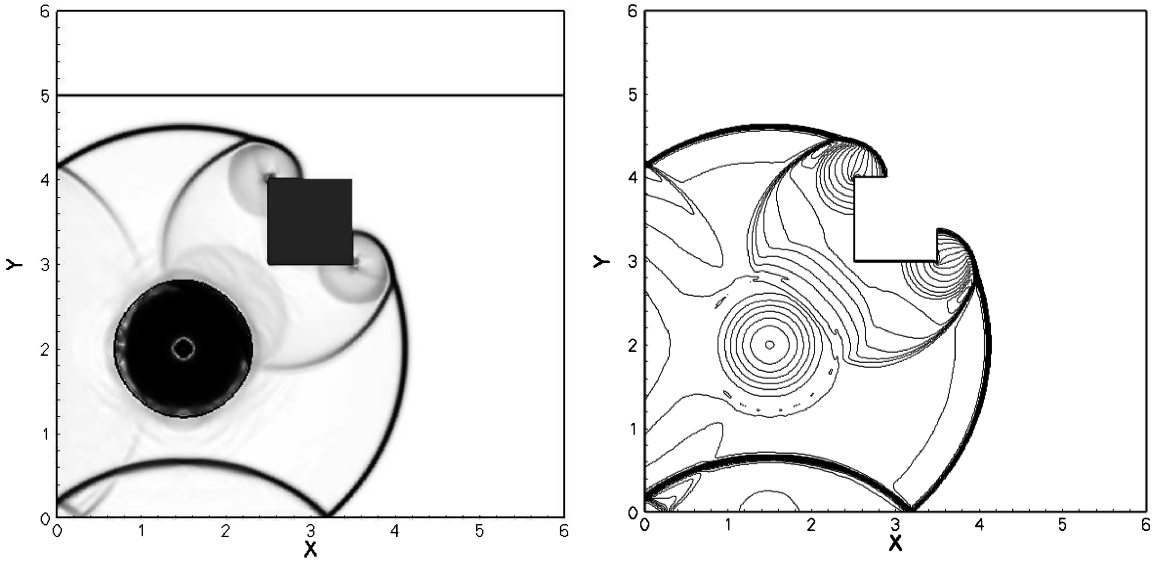

a) Numerical schlieren image at *t*=0.01 **b) Pressure contours at *t*=0.01**

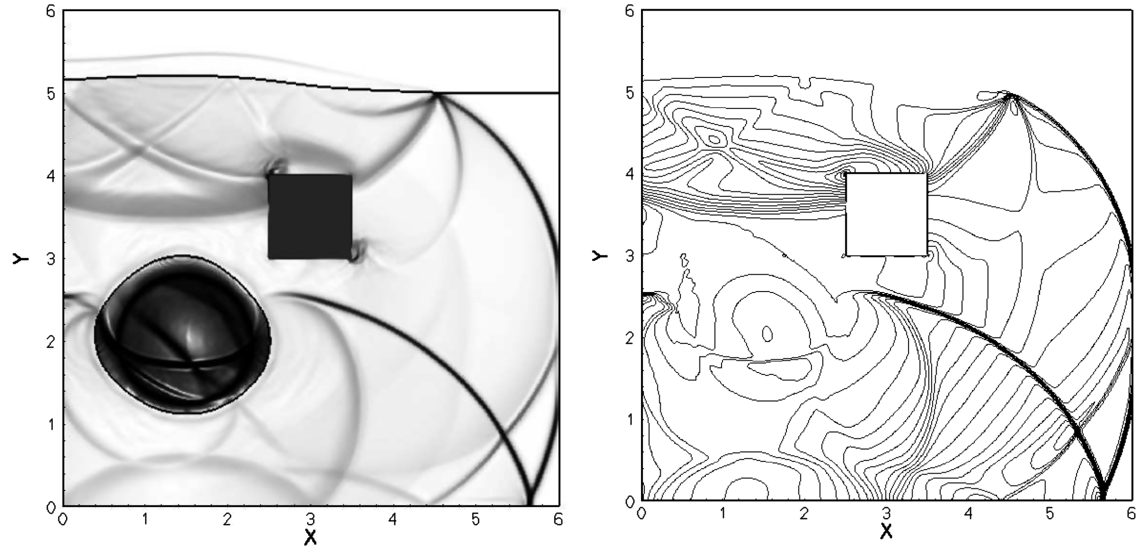

c) Numerical schlieren image at *t*=0.0197 **d) Pressure contours at *t*=0.0197**

Fig. 17 Snapshots of numerical schlieren image (left) and corresponding pressure contours (right) at different instants in time.

key features such as lateral jetting of the liquid droplet along the contact edge, the shock wave traveling in the droplet and in the surrounding air, the reflected rarefaction wave, and focusing of the rarefaction wave at the top end of the droplet are captured well. It is worth mentioning that the fine-mesh calculations shown in this example were carried out with roughly one million points (935,000 grid points), which is one-half of the number of mesh points used by Haller et al. (two million grid points), who used a front-tracking solution procedure (FronTier) due to Glimm et al. [66,67].

4. Shock Loading on a Submerged Structure Due to an Underwater Explosion

The next problem considered in this section is the evolution of an underwater explosion and its impact on a submerged structure. A square structure submerged in water is impacted by a circular shock wave generated by an explosion. The shock wave imparts severe loading on the structure that could potentially damage the structure. This is a multimaterial flow problem consisting of multiple interfaces: air–water, gas–water, and solid–water interface. For the fluid–fluid interfaces, the methodology discussed in the previous sections was adopted to define the ghost states. For the solid–fluid interface, the reflective boundary condition (RBC) augmented with a Riemann solver was used to construct the ghost field. This problem is discussed at length by Liu et al. [68]. The explosive core of 0.1 m radius is located at (1.5, 2.0) in a 6×6 m domain. The free surface separating water from air is located at $Y = 5.0$. The square structure with length $= 1.0$ m is located at the center of the domain. The flow conditions normalized with properties of water at ambient conditions are

$$(\rho, P, u, v, \gamma) = \begin{cases} (1270.0, 9000.74, 0.0, 0.0, 1.4) & \text{for the core, } \sqrt{(x-1.5)^2 + (y-2.0)^2} \le 0.1 \\ (1.0, 1.0, 0.0, 0.0, 5.5) & \text{for quiescent water, } y < 5.0 \\ (0.001, 1.0, 0.0, 0.0, 1.4) & \text{for ambient air, } y \ge 5.0 \end{cases}$$

The bottom of the domain is prescribed with reflective boundary condition and the top, right, and left boundaries are prescribed with Neumann conditions. The explosion sets off a circular shock wave that interacts with the structure and later with the free surface. The incident shock impacts first on the bottom and the left face of the square structure, resulting in a complex shock diffraction pattern, as shown in Fig. 17. Figures 17a and 17b show the shock diffracting off the structure along with the vortices produced at the top left and the bottom right corner. At this stage, the shock has not impacted the free surface. The inward-traveling expansion wave and the contact discontinuity separating the explosive core from water are also clearly visible. The shock wave reflected off the bottom wall of the domain can be seen advancing toward the explosive core. Figures 17c and 17d show the plots at a later instant in time. The shock wave has impacted the free surface and the reflected expansion wave traveling in the water medium and the transmitted shock wave in air are clearly visible. The reflected shock wave from the bottom wall of the domain has now reached the explosive core, deforming its shape.

The net horizontal and vertical force components were computed by integrating the pressure force acting on the structure. The force components exerted on the square structure are plotted are shown in Fig. 18. The horizontal and the vertical force components have the same form and they overlap with each other until $t = 0.017$. This is expected because the wave structure resulting from the initial shock impact (on the bottom and the left wall) is symmetric with respect to the structure. Later in time, the vertical force is considerably modified due to the strong reflected rarefaction wave from the free surface and hence begins to depart from the horizontal component. The moment exerted on the structure due to these forces was also computed and plotted in Fig. 18. For a quantitative comparison, the force components computed from the current simulation are compared with those obtained by Liu et al.[68]. Liu et al. used MGFM to resolve the fluid–fluid interface and symmetry-based RBC (developed by Forrer and Jeltsch [69]) for the solid–fluid interface. As shown in Fig. 19, the results from the present simulation compare very well with those of Liu et al. [68].

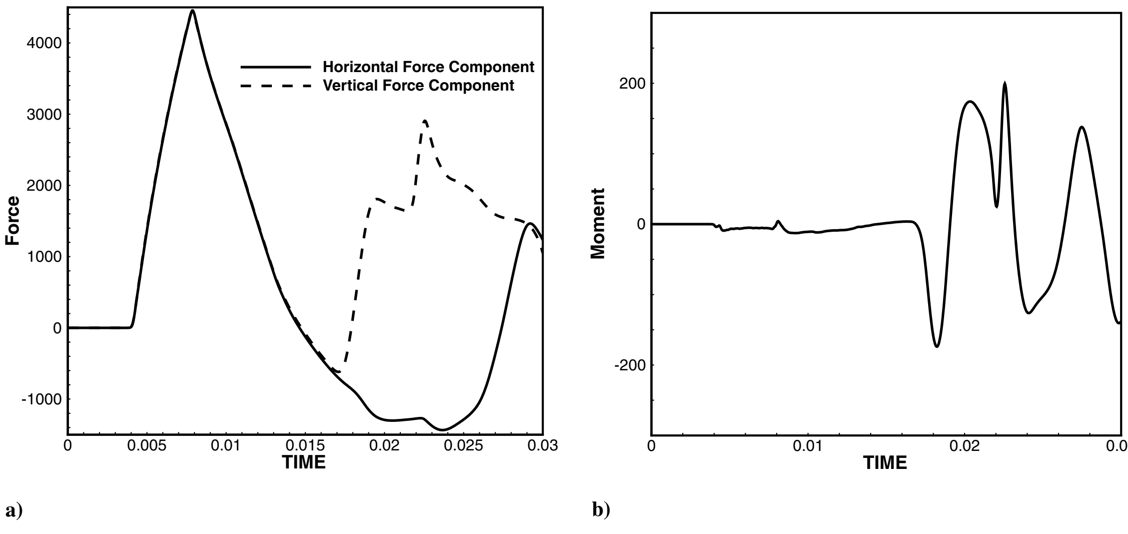

Fig. 18 Plots of a) nondimensionalized force components and b) moment exerted on the submerged square structure.

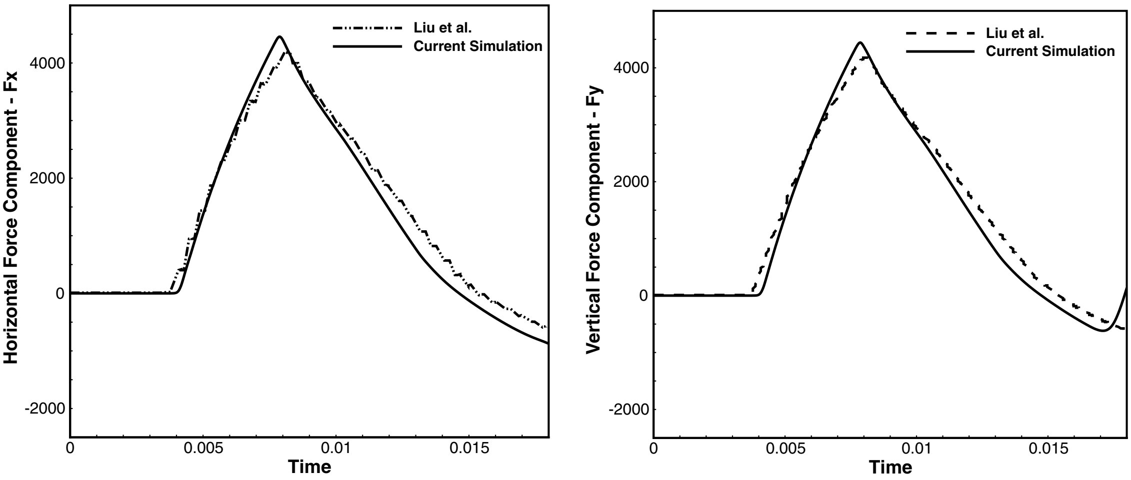

a) b)

Fig. 19 Comparison of nondimensionalized a) horizontal and b) vertical force components exerted on the submerged square structure with that of Liu et al. [68].

V. Conclusions

The interaction of strong shock waves with embedded fluid–fluid interfaces in compressible flows was studied. The interface is retained as a sharp entity by virtue of the ghost fluid method (GFM). It was shown earlier that solving a local Riemann problem at the interface alleviated the pitfalls encountered by the original GFM approach. Hence, in this work, a simple procedure to incorporate the Riemann problem at the interface was developed. The method was found to be robust in handling shocks of varied magnitude interacting with both gas–gas and gas–liquid interfaces. The (mass, momentum, and energy) conservation error analysis carried out for this method revealed that these errors are significantly attenuated and localized close to the interface. Under- and overheating errors were mitigated but not entirely eliminated by the present approach. This is due to the intrinsic nonconservative nature of the ghost fluid approach in treating sharp interfaces. The proposed method was shown to generate satisfactory solutions for several complex configurations and shocks interacting with single and multiple interface(s); shocks interacting with droplets, bubbles, and free surface have been computed. The method is currently being applied to study the dynamics of dense particulate compressible flows.

Acknowledgments

This work was supported by grants from the U.S. Air Force Office of Scientific Research, Program for Computational Mathematics (F49620-02-1-0410, Fariba Fahroo) and from the U.S. Air Force Research Laboratory, Eglin Air Force Base, Florida (F08630-03-1-0007, Michael E. Nixon).

References

[1] Haller, K. K., Ventikos, Y., and Poulikakos, D., "Computational Study of High Speed Liquid Droplet Impact," *Journal of Applied Physics*, Vol. 92, No. 5, 2002, pp. 2821–2828.
doi:10.1063/1.1495533

[2] Perigaud, G., and Saurel, R., "A Compressible Flow Model with Capillary Effects," *Journal of Computational Physics*, Vol. 209, No. 1, 2005, pp. 139–178.
doi:10.1016/j.jcp.2005.03.018

[3] Quirk, J. J., and Karni, S., "On the Dynamics of Shock Bubble Interaction," *Journal of Fluid Mechanics*, Vol. 318, 1996, pp. 129–163.
doi:10.1017/S0022112096007069

[4] Tran, L. B., and UdayKumar, H. S., "A Particle Levelset Based Sharp Interface Cartesian Grid Method for Impact, Penetration, and Void Collapse," *Journal of Computational Physics*, Vol. 193, No. 2, 2004, pp. 469–510.
doi:10.1016/j.jcp.2003.07.023

[5] Scott, S. D., Yoo, S., and Wescott, B. L., "High-Order Numerical Simulation and Modelling of the Interaction of Energetic and Inert Materials," *Combustion Theory and Modeling*, Vol. 11, No. 2, April 2007, pp. 305–332.

[6] Xu, S., Aslam, T. D., and Scott Stewart, D., "High Resolution Numerical Simulation of Ideal and Non-Ideal Compressible Reacting Flows with Embedded Internal Boundaries," *Combustion Theory and Modeling*, Vol. 1, No. 1, 1997, pp. 113–142.
doi:10.1080/713665233

[7] Grove, J. W., and Menikoff, R., "Anomalous Reflection of a Shock Wave at a Fluid Interface," *Journal of Fluid Mechanics*, Vol. 219, 1990, pp. 313–336.
doi:10.1017/S0022112090002968

[8] Shu, C. W., and Osher, S., "Efficient Implementation of Essentially Non-Oscillatory Shock Capturing Schemes 2," *Journal of Computational Physics*, Vol. 83, No. 1, 1989, pp. 32–78.
doi:10.1016/0021-9991(89)90222-2

[9] Jiang, G.-S., and Shu, C.-W., "Efficient Implementation of Weighted ENO Schemes," *Journal of Computational Physics*, Vol. 126, 1996, pp. 202–228.
doi:10.1006/jcph.1996.0130

[10] Liu, T. G., Khoo, B. C., and Wang, C. W., "Ghost Fluid Method for Compressible Gas–Water Simulation," *Journal of Computational Physics*, Vol. 204, 2005, pp. 193–221.

[11] Johnsen, E., and Colonius, T., "Implementation of WENO Schemes in Compressible Multicomponent Flow Problems," *Journal of Computational Physics*, Vol. 219, No. 2, 2006, pp. 715–732.
doi:10.1016/j.jcp.2006.04.018

[12] Karni, S., "Hybrid Multi-Fluid Algorithms," *SIAM Journal on Scientific Computing*, Vol. 17, No. 5, 1996, pp. 1019–1039.
doi:10.1137/S106482759528003X

[13] Glimm, J., Li, X. L., and Zhao, N., "Conservative Front Tracking and Level Set Algorithms," *Proceedings of the National Academy of Sciences of the United States of America*, Vol. 98, No. 25, 2001, pp. 14198–14201.
doi:10.1073/pnas.251420998

[14] Davis, S. F., "An Interface Tracking Method for Hyperbolic Systems of Conservations Laws," *Applied Numerical Mathematics*, Vol. 10, No. 6, 1992, pp. 447–472.
doi:10.1016/S0168-9274(06)80001-2

[15] Abgrall, R., "How to Prevent Pressure Oscillations in Multicomponent Flow Calculations: A Quasi Conservative Approach," *Journal of Computational Physics*, Vol. 125, No. 1, 1996, pp. 150–160.
doi:10.1006/jcph.1996.0085

[16] Abgrall, R., and Karni, S., "Computations of Compressible Multi-Fluids," *Journal of Computational Physics*, Vol. 169, No. 2, May 2001, pp. 594–623.
doi:10.1006/jcph.2000.6685

[17] Jenny, P., Muller, B., and Thomann, H., "Correction of Conservative Euler Solvers for Gas Mixtures," *Journal of Computational Physics*, Vol. 132, No. 1, 1997, pp. 91–107.
doi:10.1006/jcph.1996.5625

[18] Cocchi, J. P., and Saurel, R., "A Riemann Problem Based Method for the Resolution of Compressible Multimaterial Flows," *Journal of Computational Physics*, Vol. 137, No. 2, 1997, pp. 265–298. doi:10.1006/jcph.1997.5768

[19] Cocchi, J. P., Saurel, R., and Loraud, J. C., "Treatment of Interface Problems with Godunov-Type Schemes," *Shock Waves*, Vol. 5, No. 6, 1996, pp. 347–357. doi:10.1007/BF02434010

[20] Liu, T. G., Khoo, B. C., and Yeo, K. S., "Ghost Fluid Method for Strong Shock Impacting on Material Interface," *Journal of Computational Physics*, Vol. 190, 2003, pp. 651–681.

[21] Chang, C. H., and Liou, M. S., "A Robust and Accurate Approach to Computing Compressible Multiphase Flow: Stratified Flow Model and AUSM+—Up Scheme," *Journal of Computational Physics*, Vol. 225, No. 1, 2007, pp. 840–873. doi:10.1016/j.jcp.2007.01.007

[22] Marquina, A., and Mulet, P., "A Flux-Split Algorithm Applied to Conservative Models for Multicomponent Compressible Flows," *Journal of Computational Physics*, Vol. 185, No. 1, 2003, pp. 120–138. doi:10.1016/S0021-9991(02)00050-5

[23] Hong, J. M., Shinar, T., Kang, M., and Fedkiw, R., "On Boundary Condition Capturing for Multiphase Interfaces," *Journal of Scientific Computing*, Vol. 31, Nos. 1–2, 2007, pp. 99–125. doi:10.1007/s10915-006-9120-x

[24] Marella, S., Krishnan, S., Liu, H., and UdayKumar, H. S., "Sharp Interface Cartesian Grid Method 1: An Easily Implemented Technique for 3D Moving Boundary Computations," *Journal of Computational Physics*, Vol. 210, No. 1, 2005, pp. 1–31. doi:10.1016/j.jcp.2005.03.031

[25] Mittal, R., "Immersed Boundary Methods," *Annual Review of Fluid Mechanics*, Vol. 37, 2005, pp. 239–261. doi:10.1146/annurev.fluid.37.061903.175743

[26] Sussman, M., Smith, K. M., Hussaini, M. Y., Ohta, M., and Zhi-Wei, R. "A Sharp Interface Method for Incompressible Two-Phase Flows," *Journal of Computational Physics*, Vol. 221, No. 2, 2007, pp. 469–505. doi:10.1016/j.jcp.2006.06.020

[27] Fedkiw, R., "Coupling an Eulerian Fluid Calculation to a Lagrangian Solid Calculation with the Ghost Fluid Method," *Journal of Computational Physics*, Vol. 175, No. 1, 2002, pp. 200–224. doi:10.1006/jcph.2001.6935

[28] Fedkiw, R. P., Aslam, T. D., Merriman, B., and Osher, S., "A Non Oscillatory Eulerian Approach to Interfaces in Multimaterial Flows (The Ghost Fluid Method)," *Journal of Computational Physics*, Vol. 152, No. 2, 1999, pp. 457–492. doi:10.1006/jcph.1999.6236

[29] Nourgaliev, R. R., Dinh, T. N., and Theofanous, T. G., "The Characteristic Based Matching (CBM) Method for Compressible Flow in Complex Geometries," 41st AIAA Aerospace Sciences Meeting and Exhibit, Reno, NV, AIAA Paper 2003-0247, Jan. 2003.

[30] Nourgaliev, R. R., Dinh T. N., and Theofanous, T. G., "The Characteristic Based Matching (CBM) Method for Compressible Flow with Moving Boundaries and Interfaces," *Journal of Fluids Engineering*, Vol. 126, 2004, pp. 586–604. doi:10.1115/1.1778713

[31] Fedkiw, R. P., Marquina, A., and Merriman, B., "An Isobaric Fix for the Overheating Problem in Multimaterial Compressible Flows," *Journal of Computational Physics*, Vol. 148, No. 2, 1999, pp. 545–578. doi:10.1006/jcph.1998.6129

[32] Fedkiw, R. P., Aslam, T. D., and Xu, S., "The Ghost Fluid Method for Deflagration and Detonation Discontinuities," *Journal of Computational Physics*, Vol. 154, No. 2, 1999, pp. 393–427. doi:10.1006/jcph.1999.6320

[33] Caiden, R., Fedkiw, R. P., and Anderson, C., "A Numerical Method for Two-Phase Flow Consisting of Separate Compressible and Incompressible Regions," *Journal of Computational Physics*, Vol. 166, No. 1, 2001, pp. 1–27. doi:10.1006/jcph.2000.6624

[34] Aslam, T. D., "A Level Set Algorithm for Tracking Discontinuities in Hyperbolic Conservation Laws 1: Scalar Equations," *Journal of Computational Physics*, Vol. 167, No. 2, 2001, pp. 413–438. doi:10.1006/jcph.2000.6686

[35] Aslam, T. D., "A Level Set Algorithm for Tracking Discontinuities in Hyperbolic Conservation Laws 2: Systems of Equations," *Journal of Scientific Computing*, Vol. 19, Nos. 1–3, 2003, pp. 37–62. doi:10.1023/A:1025387405273

[36] Hu, X. Y., and Khoo, B. C., "An Interface Interaction Method for Compressible Multi-Fluids," *Journal of Computational Physics*, Vol. 198, 2004, pp. 35–64.

[37] Wang, C. W., Liu, T. G., and Khoo, B. C., "A Real Ghost Fluid Method for the Simulation of Multimedium Compressible Flow," *SIAM Journal on Scientific Computing*, Vol. 28, No. 1, 2006, pp. 278–302. doi:10.1137/030601363

[38] Menikoff, R., "Errors When Shock Waves Interact Due to Numerical Shock Width," *SIAM Journal on Scientific Computing*, Vol. 15, No. 5, 1994, pp. 1227–1242. doi:10.1137/0915075

[39] Noh, W. F., "Errors for Calculations of Strong Shocks Using an Artificial Viscosity and an Artificial Heat Flux," *Journal of Computational Physics*, Vol. 72, No. 1, 1987, pp. 78–120. doi:10.1016/0021-9991(87)90074-X

[40] Sambasivan, S., and UdayKumar, H. S., "Ghost Fluid Method for Strong Shock Interactions Part 2: Immersed Solid Boundaries," *AIAA Journal*, Vol. 47, No. 12, 2009, pp. 2923–2937. doi:10.2514/1.43153

[41] Harlow, F., and Amsden, A., "Fluid Dynamics," Los Alamos National Lab., Monograph LA-4700, Los Alamos, NM, 1971.

[42] Menikoff, M. and Plohr, B. J., "The Riemann Problem for Fluid Flow of Real Materials," *Reviews of Modern Physics*, Vol. 61, No. 1, Jan. 1989, pp. 75. doi:10.1103/RevModPhys.61.75

[43] Osher, S., and Sethian, J. A., "Fronts Propagating with Curvature Dependent Speed Algorithms Based on Hamilton-Jacobi," *Journal of Computational Physics*, Vol. 79, No. 1, 1988, pp. 12–49. doi:10.1016/0021-9991(88)90002-2

[44] Sethian, J. A., "Evolution, Implementation, Application of Levelsets and Fast Marching Methods for Advancing Fronts," *Journal of Computational Physics*, Vol. 169, No. 2, 2001, pp. 503–555. doi:10.1006/jcph.2000.6657

[45] Sethian, J. A., and Smereka, P., "Levelset Methods for Fluid Interfaces," *Annual Review of Fluid Mechanics*, Vol. 35, 2003, pp. 341–372. doi:10.1146/annurev.fluid.35.101101.161105

[46] Sethian, J. A., "Level Set Methods and Fast Marching Methods: Evolving Interfaces in Computational Geometry," *Fluid Mechanics, Computer Vision, and Materials Science*, 2nd ed., Cambridge Univ. Press, New York, 1999.

[47] Glimm, J., Marchesin, D., and O. McBryan, "A Numerical Method for Two Phase Flow with an Unstable Interface," *Journal of Computational Physics*, Vol. 39, No. 1, 1981, pp. 179–200. doi:10.1016/0021-9991(81)90144-3

[48] Toro, E. F., *Riemann Solvers and Numerical Methods for Fluid Dynamics—A Practical Introduction*, 2nd ed., Springer, New York, 1997.

[49] Aslam, T. D., "A Partial Differential Equation Approach to Multidimensional Extrapolation," *Journal of Computational Physics*, Vol. 193, No. 1, 2004, pp. 349–355. doi:10.1016/j.jcp.2003.08.001

[50] Liu, X. D., and Osher, S., "Convex ENO High Order Multidimensional Schemes Without Field by Filed Decomposition or Staggered Grids," *Journal of Computational Physics*, Vol. 142, 1998, pp. 304–330.

[51] Nguyen, D. Q., Gibou, F., and Fedkiw R., "A Fully Conservative Ghost Fluid Method and Stiff Detonation Waves," *12th International Detonation Symposium*, San Diego, CA, Aug. 2002.

[52] Hu, X. Y., Khoo, B. C., Adams, N. A., and Huang, F. L., "A Conservative Interface Method for Compressible Flows," *Journal of Computational Physics*, Vol. 219, No. 2, May 2006, pp. 553–578. doi:10.1016/j.jcp.2006.04.001

[53] Henderson, L. F., "On the Refraction of Shock Waves," *Journal of Fluid Mechanics*, Vol. 198, 1989, pp. 365–386. doi:10.1017/S0022112089000170

[54] Langseth, J. O., and Leveque, R. J., "A Wave Propagation Method for Three Dimensional Hyperbolic Conservation Laws," *Journal of Computational Physics*, Vol. 165, 2000, pp. 125–166.

[55] Chalmersa, J. W., Hodsona, S. W., Winklera, K. H. A., Woodward, P. R., and Zabusky, N. J., "Shock-Bubble Interactions: Generation and Evolution of Vorticity in Two-Dimensional Supersonic Flows," *Fluid Dynamics Research*, Vol. 3, Nos. 1–4, 1988, pp. 392–394. doi:10.1016/0169-5983(88)90098-6

[56] Pittard, J. M., Hartquist, T. W., and J. Dyson, E., "Self-Similar Evolution of Wind-Blown Bubbles with Mass Loading by Hydrodynamic Ablation," *Astronomy and Astrophysics*, Vol. 373, No. 3, 2001, pp. 1043–1055. doi:10.1051/0004-6361:20010673

[57] Jamaluddin, A. R., Ball, G. J., and Leighton, T. G., "Free-Lagrange Simulations of Shock/Bubble Interaction in Shock Wave Lithotripsy," *Second International Conference on Computational Fluid Dynamics*, 2002.

[58] Haas, J. F., and Sturtevant, B., "Interaction of Weak Shock Waves with Cylindrical and Spherical Inhomogeneities," *Journal of Fluid Mechanics*, Vol. 181, 1987, pp. 41–76.
doi:10.1017/S0022112087002003

[59] Bagabir, A., and Drikakis, D., "Mach Number Effects on Shock-Bubble Interaction," *Shock Waves*, Vol. 11, No. 3, 2001, pp. 209–218.
doi:10.1007/PL00004076

[60] Abd-El-Fattah, A. M., and Henderson, L. F., "Shock Waves at a Slow-Fast Gas Interface," *Journal of Fluid Mechanics*, Vol. 89, 1978, pp. 79–95.
doi:10.1017/S0022112078002475

[61] Krishnan, S., "An Adaptively Refined Cartesian Grid Method for Moving Boundary Problems Applied to Biomedical Systems," Ph.D. Thesis, Univ. of Iowa, Ames, IA, 2006.

[62] Cheng, D., Trapaga, G., McKelliget, J. W., and Lavernia, E. J., "Mathematical Modelling of High Velocity Oxygen Fuel Thermal Spraying of Nanocrystalline Materials: An Overview," *Modelling and Simulation in Materials Science and Engineering*, Vol. 11, No. 1, 2003, pp. 1–31.
doi:10.1088/0965-0393/11/1/201

[63] Haller, K. K., "High-Velocity Impact of a Liquid Droplet on a Rigid Surface: The Effect of Liquid Compressibility," Ph.D. Thesis, Swiss Federal Inst. of Technology, Zurich, 2002.

[64] Haller, K. K., Poulikakos, D., Ventikos, Y., and Monkewitz, P., "Shock Wave Formation in Droplet Impact on a Rigid Surface: Lateral Liquid Motion and Multiple Wave Structure in the Contact Line Region," *Journal of Fluid Mechanics*, Vol. 490, 2003, pp. 1–14.
doi:10.1017/S0022112003005093

[65] Haller, K. K., Ventikos, Y., and Poulikakos, D., "Wave Structure in the Contact Line Region During High Speed Droplet Impact on a Surface: Solution of the Riemann Problem for the Stiffened Gas Equation of State," *Journal of Applied Physics*, Vol. 93, No. 5, 2003, pp. 3090–3097.
doi:10.1063/1.1543649

[66] Glimm, J., Grove, J. W., Li, X., Shyue, K. M., Zeng, Y., and Zhang, Q., "Three-Dimensional Front Tracking," *SIAM Journal on Scientific Computing*, Vol. 19, No. 3, 1998, pp. 703–727.
doi:10.1137/S1064827595293600

[67] Glimm, J., Klingenberg, C., O. McBryan, Plohr, B., Sharp, D., and Yaniv, S., "Front Tracking and Two-Dimensional Riemann Problems," *Advances in Applied Mathematics*, Vol. 6, No. 3, 1985, pp. 259–290.
doi:10.1016/0196-8858(85)90014-4

[68] Liu, T. G., Khoo, B. C., Yeo, K. S., and Wang, C., "Underwater Shock-Free Surface-Structure Interaction," *International Journal for Numerical Methods in Engineering*, Vol. 58, 2003, pp. 609–630.

[69] Forrer, H., and Jeltsch, R., "A Higher Order Boundary Treatment for Cartesian Grid Methods," *Journal of Computational Physics*, Vol. 140, No. 2, 1998, pp. 259–277.
doi:10.1006/jcph.1998.5891

K. Anderson
Associate Editor